Catalysis Today 150 (2010) 100–106

Contents lists available at ScienceDirect

Catalysis Today

journal homepage: www.elsevier.com/locate/cattod

Catalytic chemical vapour deposition of carbon nanotubes using Fe-doped alumina catalysts

Pezhman Zarabadi-Poor [a], Alireza Badiei [a,*], Ali Akbar Yousefi [b], Bradley D. Fahlman [c], Alireza Abbasi [a]

[a] School of Chemistry, University College of Science, University of Tehran, Tehran, Iran
[b] Institute for Colorants, Paints and Coatings, P.O. Box 16765-654, Tehran, Iran
[c] Department of Chemistry, Central Michigan University, Mount Pleasant, MI, USA

ARTICLE INFO

Article history:
Available online 31 July 2009

Keywords:
CVD
Carbon nanotubes
Carbon nanoribbons
Alumina
Supported catalysts
Fe/Al_2O_3

ABSTRACT

The catalytic chemical vapour deposition (CCVD) of carbon nanotubes onto Fe-doped alumina catalysts, with varying iron concentrations and reaction times is described. Methane was used as a carbon source, and nanostructural growth was afforded at 1000 °C. Characterization of alumina-supported iron catalysts was done using N_2 adsorption–desorption measurement and X-ray diffraction. Scanning electron microscopy (SEM), transmission electron microscopy (TEM), thermogravimetric analysis (TGA) and Raman spectroscopy were used for characterization of resultant carbon nanotubes (CNTs). The SEM images indicate that diameter and length of as-produced CNTs depends on both iron content of the catalyst and reaction time; with lower iron concentrations, longer and thinner nanotubes were obtained. The yield of products was investigated by TGA, and showed that increasing the catalyst iron content and reaction time directly affect the amount of formed product.

1. Introduction

Since the discovery of carbon nanotubes (CNTs) by Iijima [1], they have attracted a lot of interest due to their remarkable physical and chemical properties [2]. These properties make CNTs suitable for applications in hydrogen storage devices [3,4], field emission tips [5], nanotweezers [6], chemical sensors [7], etc. A variety of methods have been developed for the synthesis of CNTs; for example, arc discharge [8,9], laser ablation [10] and catalytic chemical vapour deposition (CCVD) [11,12]. The latter one, CCVD, in comparison with the other methods, is a simple and economic technique for synthesizing CNTs at moderate temperature [13]. In the CCVD method, a feedstock carbon source (such as methane, ethane, CO and ROH) is heated to 700–1000 °C over a transition metal catalyst to promote carbon nanotube growth [14]. Usually, this process employs iron, cobalt, or nickel-supported catalysts [15] prepared by impregnation [16], co-precipitation [17], or sol–gel [18]. High surface area and isolated channels are desirable properties in silica and alumina as catalyst supports, preventing coalescence of metal particles during synthesis [13].

Alumina-supported metal catalysts for the synthesis of CNTs have been widely reported. The high-yield synthesis of CNTs was reported by using C_2H_6 as a carbon feedstock over Fe/Al_2O_3 catalyst [19]. The simultaneous production of CNTs and hydrogen were investigated from decomposition of ethanol in presence of Fe/Al_2O_3 [20]. Wang et al. developed a nano-agglomerate fluidized-bed reactor in which the continuous decomposition of ethylene gas on an Fe/alumina catalyst at 700 °C produces a few kilograms of multi-walled carbon nanotubes per hour with a reported purity of 70% [21]. Dikonimos Makris et al. reported CNT synthesis using commercial alumina-supported nickel catalysts. They have optimized the reaction parameters as following: 30 min of reaction time, 600 °C of growth temperature, 100 mbar of pressure and 10:70 ratio between hydrogen and methane in the reaction feedstock [22]. In other research in this field, Nagaraju et al. reported that a best yield of MWNTs is obtained on hydrated alumina prepared from aluminium isopropoxide and containing a mixture of Fe and Co on it [23]. Also, a kinetic study in the synthesis of multi-walled carbon nanotubes using bi-metallic alumina-supported catalysts was done by Pirard et al. They have reported that in best model rate determining step is the elimination of the first atom of hydrogen from the adsorbed ethylene [24].

Herein, we report the CCVD synthesis of CNTs using an Fe/Al_2O_3 catalyst, and methane as a carbon source. We will focus on the influence of the Fe concentration of the alumina-supported catalyst and reaction time on the resultant morphology and yield of CNTs.

2. Experimental

2.1. Materials

Iron(III) nitrate nonahydrate (Merck), methanol (Merck), methane (99.99%) and alumina (Djajarm-Iran, specific surface

* Corresponding author. Tel.: +98 21 61112614; fax: +98 21 66405141.
E-mail address: abadiei@khayam.ut.ac.ir (A. Badiei).

0920-5861/$ – see front matter © 2009 Elsevier B.V. All rights reserved.
doi:10.1016/j.cattod.2009.06.019

Table 1
Prepared catalysts with corresponding concentration of iron(III) nitrate solutions.

Catalysts	Concentration of Fe solutions (M)
$Fe_{0.02}$–alumina	0.02
$Fe_{0.05}$–alumina	0.05
$Fe_{0.07}$–alumina	0.07
$Fe_{0.10}$–alumina	0.10

area: 55 m^2/g and pore diameter: 9 nm) were used as received.

2.2. Synthesis of catalysts

Catalysts were prepared according to Ref. [25] with slight modification. A series of iron(III) nitrate solutions (0.02, 0.05, 0.07 and 0.10 M) were prepared in methanol. In a typical procedure, alumina powder (1.0 g) was stirred with 0.02 M iron(III) nitrate solution (30 mL) for 2 h at room temperature. After stirring, the solvent was removed in a rotary evaporator. Finally, the resultant solid was dried at 150 °C overnight to yield a brown solid that was ground into a finely divided powder using a mortar and pestle. Table 1 shows all prepared catalysts.

2.3. Synthesis of CNTs

In a typical synthesis [25], the catalyst powder was placed into a quartz tube fitted within a horizontal furnace and the temperature was increased to 1000 °C under argon gas. After temperature equilibration was reached, methane gas (CH_4 to Ar ratio of 90:10) was introduced into the quartz tube for a certain reaction time (30, 60, 90, and 120 min). Herein, we refer to the grown CNTs as C_xNT_y (where: x represents the catalyst concentration (in mol/L), and y represents reaction time).

2.4. Characterization methods

N_2 adsorption–desorption isotherms were measured using BELSORP-miniII at liquid nitrogen temperature (77 K). All samples were degassed at 300 °C for 3 h under inert gas flow prior analysis. The specific surface area were evaluated using the Brunauer–Emmett–Teller (BET) method, and pore size distributions were calculated using the Barret–Joyner–Halenda (BJH) model on the desorption branch. X-ray powder diffraction (XRD) patterns were obtained on a Philips X'PERT diffractometer using Cu Kα radiation at 40 kV and 40 mA. Scanning electron microscopy (SEM) was carried out on a LEO 1455VP microscope. Transmission electron microscopy (TEM) was performed on a LEO 912AB under an accelerated voltage of 120 kV. Samples were dispersed in ethanol using an ultrasonic bath, and a drop placed on a lacey carbon-coated copper grid for analysis. Thermogravimetric analysis (TGA) was carried out in PerkinElmer Pyris Diamond instrument from ambient temperature to 1000 °C, using a ramp rate of 10 °C/min. Micro-Raman spectra were recorded using a Renishaw system 1000 spectrometer, equipped with Leica DMLM microscope, a 25 mW diode laser (782 nm), and a Peltier-cooled CCD detector.

3. Results and discussion

3.1. Catalysts characterization

N_2 adsorption-desorption isotherms of catalysts are given in Fig. 1. As it seen in Fig. 1, the shape of isotherms is similar to type IV standard isotherms and show mesoporosity in the alumina and iron-doped alumina. The height of isotherms decrease with increasing the iron content of catalysts and the shape of them deform. This can be related to the insertion of iron in the structure of alumina.

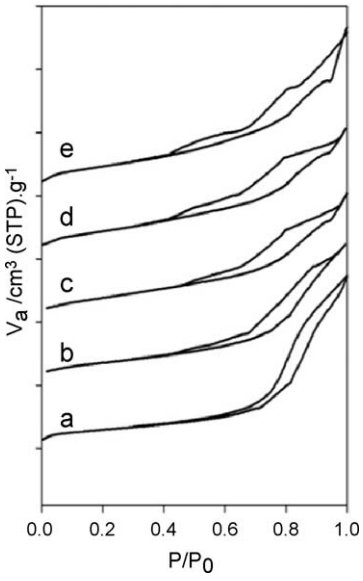

Fig. 1. N_2 adsorption-desorption isotherms of (a) alumina, (b) $Fe_{0.02}$–alumina, (c) $Fe_{0.05}$–alumina, (d) $Fe_{0.07}$–alumina and (e) $Fe_{0.10}$–alumina.

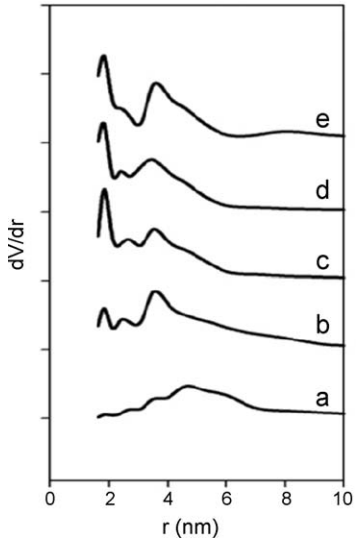

Fig. 2. BJH pore size distributions of (a) alumina, (b) $Fe_{0.02}$–alumina, (c) $Fe_{0.05}$–alumina, (d) $Fe_{0.07}$–alumina and (e) $Fe_{0.10}$–alumina.

The BJH pore size distributions of alumina and catalysts are given in Fig. 2. As it seen in BJH pore size distribution of alumina (a), there is a broad peak in the curve that this is representative for the existence of one type pore with wide distribution in the alumina structure. For the iron-doped alumina catalysts (b–e), there are two major narrow peaks that shift to smaller diameters. It can be concluded that there

Table 2
Specific surface area (S_{BET}) and pore diameters of alumina and catalysts obtained using BET and BJH methods, respectively.

Samples	S_{BET} (m^2/g)	Pore diameter (nm)
Alumina	52.3	9.20
$Fe_{0.02}$–alumina	63.8	7.04
$Fe_{0.05}$–alumina	72.9	3.72
$Fe_{0.07}$–alumina	80.5	3.72
$Fe_{0.10}$–alumina	84.3	3.72

are more than one type of pores in these systems. According to the pore size distribution of alumina, it can be assumed that due to the insertion of iron in the alumina structure, the structure of pores in the alumina is deformed and new pores are formed.

Increased specific surface areas and decreased pore diameters with iron content increasing (Table 2) can be utilized to confirm above opinion. For further discussion, it can be assumed that after iron insertion into the alumina structure, Fe sites agglomerate and form new pores inside primary pores. Consequently, specific surface area is increasing due to the formation of new surfaces inside the primary pores and pore diameter is decreasing due to the formation of Fe agglomerates.

The XRD patterns of alumina, $Fe_{0.02}$–alumina, and $Fe_{0.07}$–alumina are shown in Fig. 3. The shapes of patterns in these samples are similar. It can be concluded that insertion of iron did not affect the basic structure of alumina and it is approximately retained. The intensity of peaks is decreased with iron content increasing. It can be assumed that substitutional doping of Fe in the lattice results in more disorder, and less overall crystallinity.

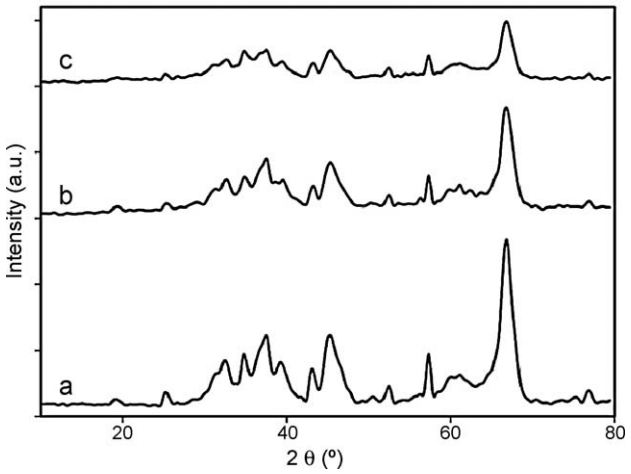

Fig. 3. XRD patterns of (a) alumina, (b) $Fe_{0.02}$–alumina and (c) $Fe_{0.07}$–alumina.

3.2. Carbon nanotubes characterization

Morphological assessment of the as-grown CNTs was done by SEM. Fig. 4 shows SEM images of C_xNT_{60} samples with different concentrations of iron on the alumina-supported catalysts, for a 60 min reaction time. It is seen that the lengths and diameters of CNTs depends on the iron content of the catalyst. In particular, longer and thinner CNTs are observed for lower concentrations of

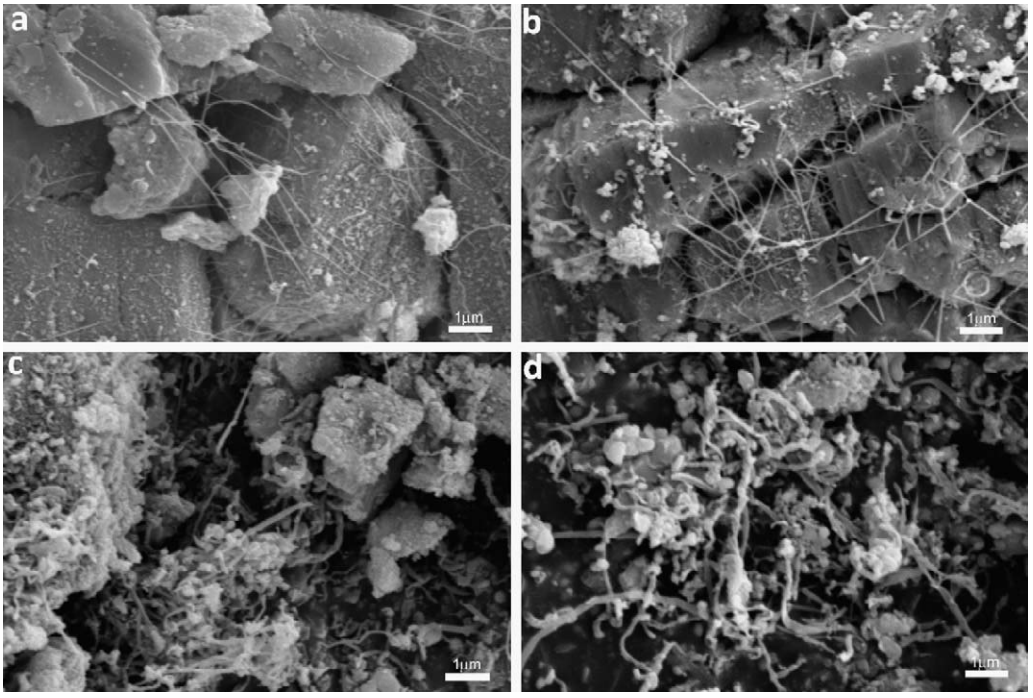

Fig. 4. SEM images of synthesized carbon nanotubes using [Fe] catalyst concentrations of (a) 0.02 M, (b) 0.05 M, (c) 0.07 M and (d) 0.10 M for a reaction time of 60 min.

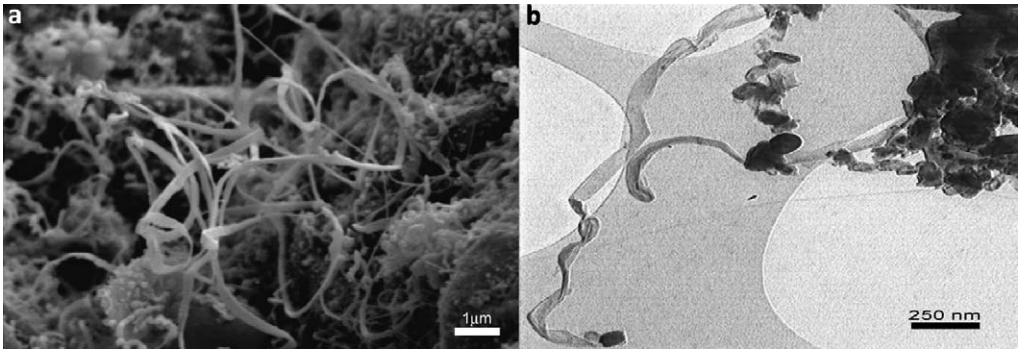

Fig. 5. (a) SEM and (b) TEM images of synthesized carbon nanoribbons with a 0.05 M [Fe] catalyst for a reaction time of 120 min.

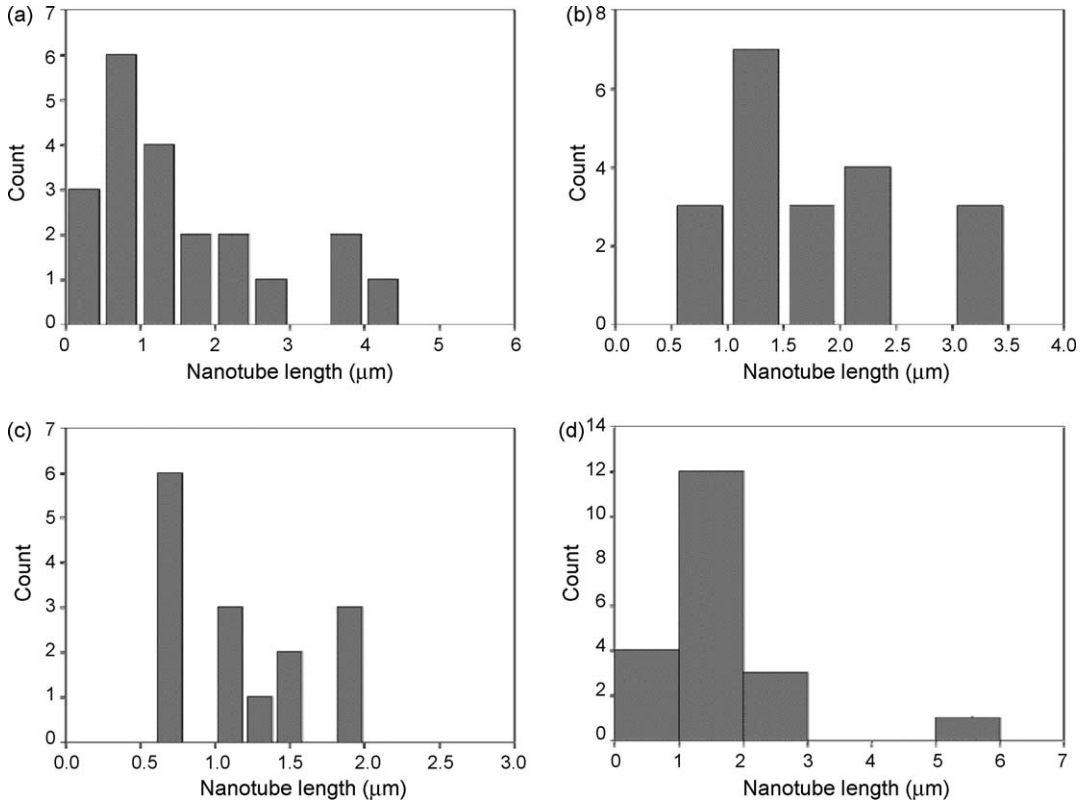

Fig. 6. Histograms of measured length for the synthesized carbon nanotubes using [Fe] catalyst concentrations of (a) 0.02 M, (b) 0.05 M, (c) 0.07 M and (d) 0.10 M for a reaction time of 60 min.

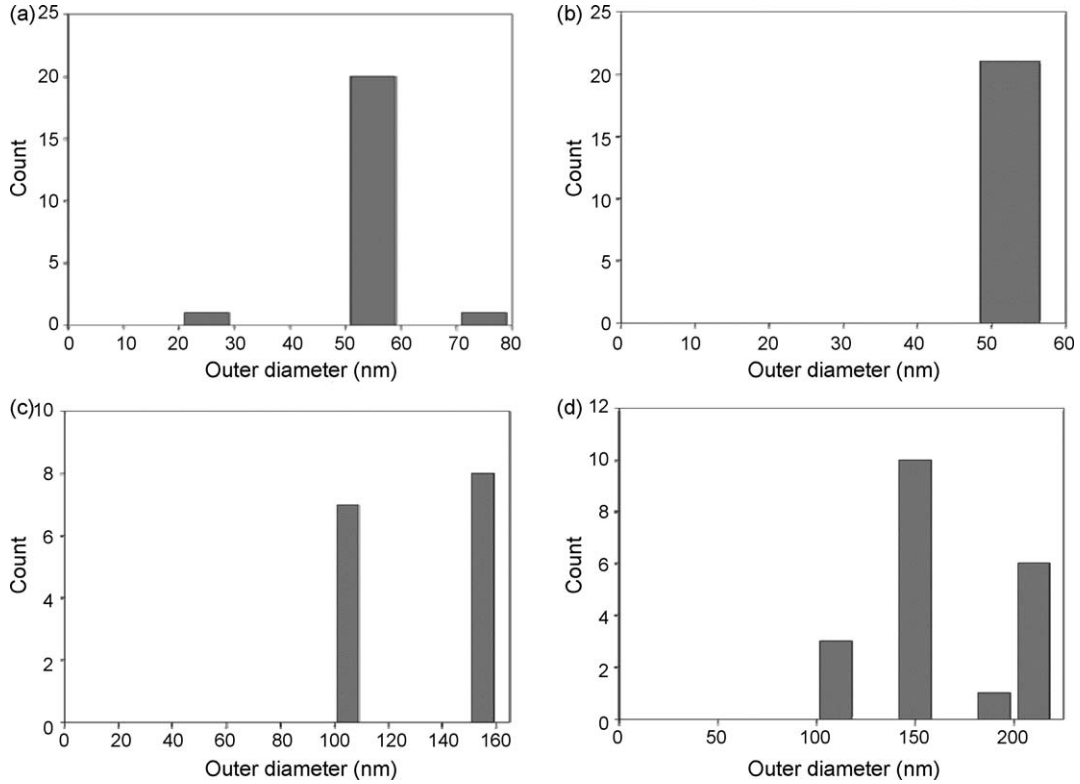

Fig. 7. Histograms of measured diameter for the synthesized carbon nanotubes using [Fe] catalyst concentrations of (a) 0.02 M, (b) 0.05 M, (c) 0.07 M and (d) 0.10 M for a reaction time of 60 min.

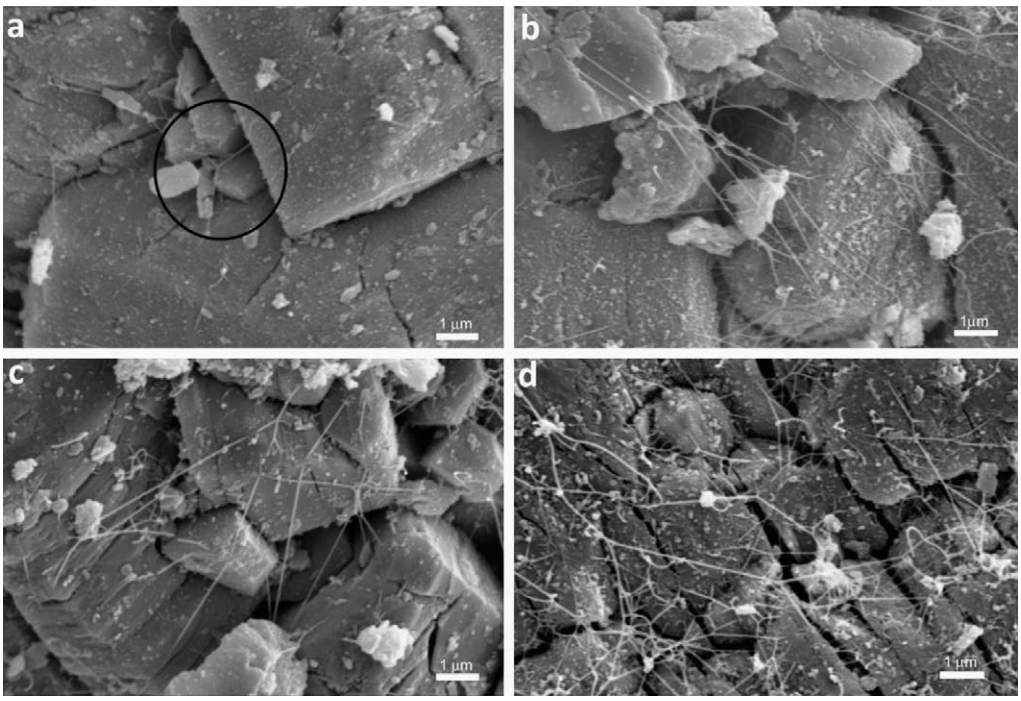

Fig. 8. SEM images of synthesized carbon nanotubes using a 0.02 M [Fe] catalyst for reaction times of (a) 30, (b) 60, (c) 90 and (d) 120 min.

iron—*i.e.*, diameters of C_xNT_{60} increase from 50 to 200 nm with increasing iron concentration. These results support the prevailing mechanistic theory of vapour–liquid–solid (VLS) for nanostructural carbon growth. That is, with lower iron concentrations, smaller Fe nanoparticles are formed on the alumina catalyst, which gives rise to smaller diameter nanotubes.

In addition to length/diameter effects, Fig. 4 also shows that increasing Fe concentrations gives rise to more complicated morphologies of resultant CNTs. Fig. 5 shows SEM and TEM images of formed carbon nanoribbons obtained in the $C_{0.05}NT_{120}$ process. This type of nanostructure was observed for higher iron concentrations, observed for [Fe] of 0.05–0.10 M.

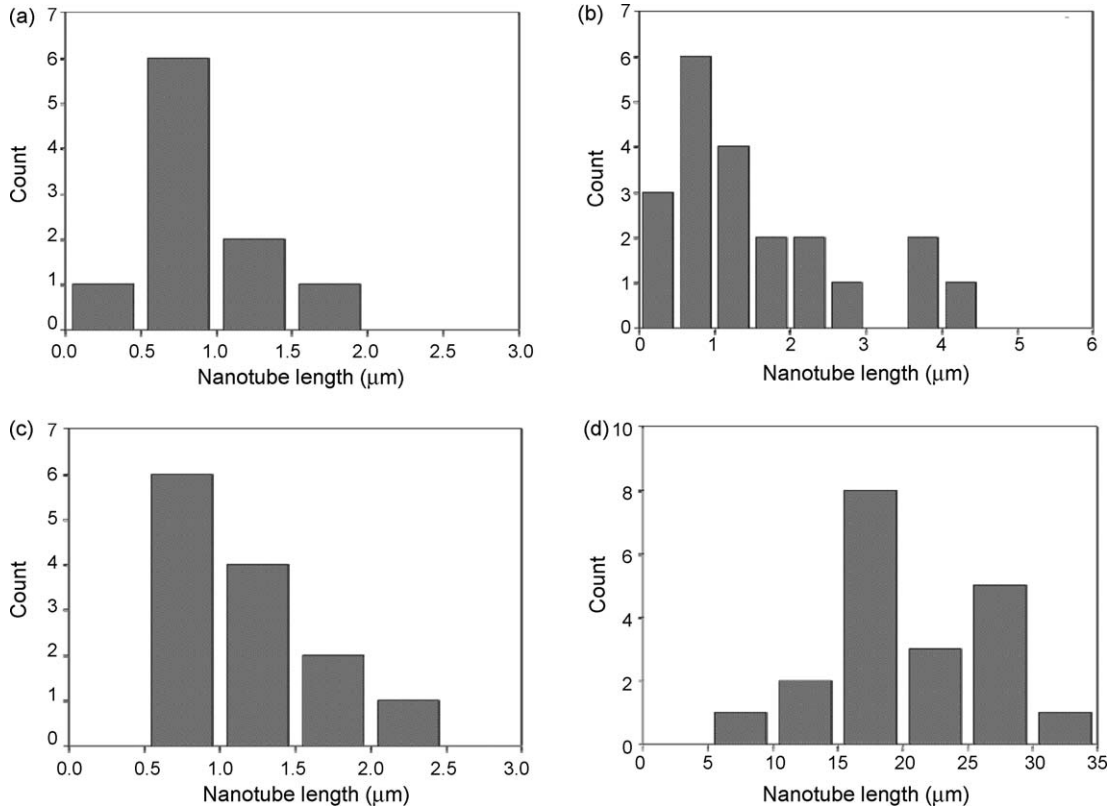

Fig. 9. Histograms of measured length for the synthesized carbon nanotubes using a 0.02 M [Fe] catalyst for reaction times of (a) 30, (b) 60, (c) 90 and (d) 120 min.

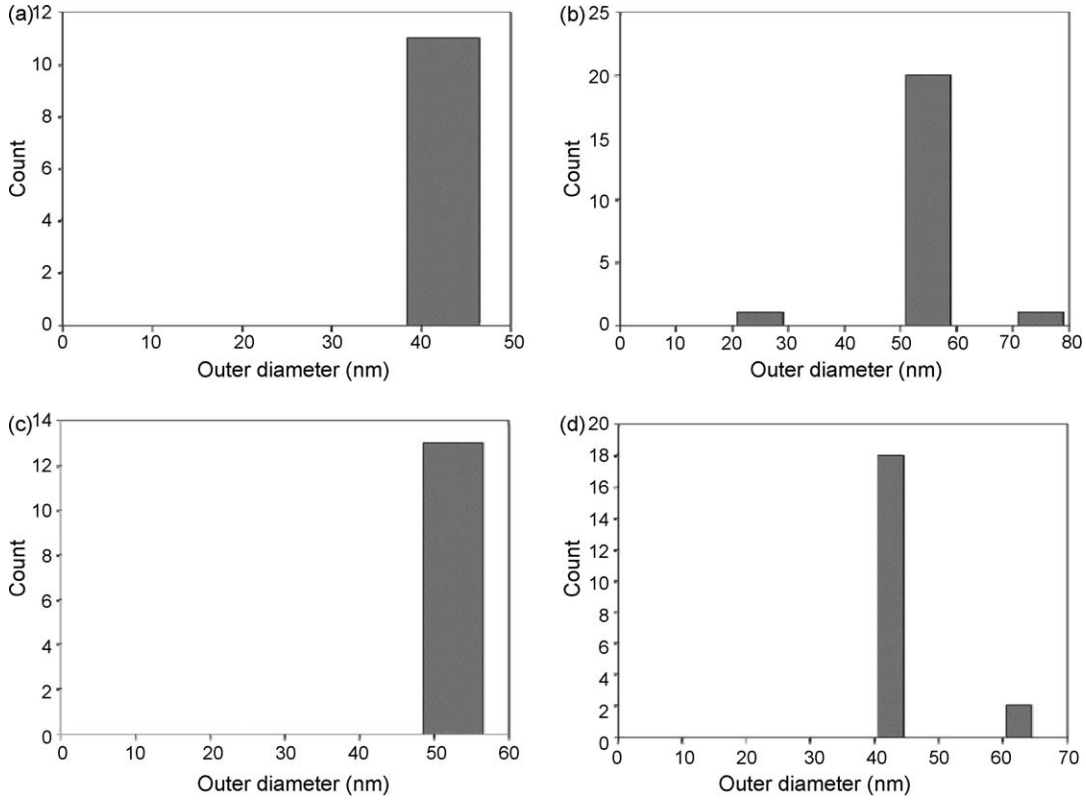

Fig. 10. Histograms of measured diameter for the synthesized carbon nanotubes using a 0.02 M [Fe] catalyst for reaction times of (a) 30, (b) 60, (c) 90 and (d) 120 min.

This suggests that as the iron concentration increases, the larger crystal facets of the alumina-supported Fe nanoparticle catalyst sites become more influential in directing the precipitation of carbon units from the supersaturated molten Fe nanoparticle catalyst sites, yielding a flattened nanostructure rather than a tubular array. We are continuing our investigations to probe the mechanistic details of this interesting morphology in more detail.

Figs. 6 and 7 show the histograms of measured length and diameter for as-grown C_xNT_{60} samples, respectively. As it seen in Fig. 6, most of the CNTs have a length of 1–2 μm. About the outer diameter of CNTs (Fig. 7), in $C_{0.02}NT_{60}$ and $C_{0.05}TN_{60}$ most of them have a diameter of 50–60 nm. For the $C_{0.07}TN_{60}$ sample, CNTs are grouped in two major groups with a diameter of 100–110 and 150–160 nm. Most of CNTs in the $C_{0.10}NT_{60}$ sample have a diameter of above 150 nm. It can be concluded that iron content increasing in catalysts did not affect the length of as-synthesized CNTs but effectively increased the diameter of them. It can be supposed that size of agglomerated Fe sites is increased with iron content increasing. Thus, diameter of grown CNTs over these sites is increased.

Fig. 8 shows SEM images of $C_{0.02}NT_y$ from different reaction times. It is observed that the yield and diameter of CNTs are both enhanced with increasing reaction times, with the onset of CNT growth for $C_{0.02}NT_y$ occurring at *ca.* 30 min. This provides feedback regarding the required nucleation threshold time required to supersaturate the catalytic Fe nanoparticles. We are currently evaluating the relationship of the growth onset temperature with Fe concentrations.

The corresponding histograms of measured length and diameter for the samples in Fig. 8 are given in Figs. 9 and 10, respectively. For the $C_{0.02}NT_{30}$, $C_{0.02}NT_{60}$, and $C_{0.02}NT_{90}$ samples, length for the most of the CNTs is *ca.* 1 μm. Most of CNTs in $C_{0.02}NT_{120}$ have a length of 15–20 μm. It can be resulted from long reaction time. As it seen in Fig. 10, for all four samples that diameter of CNTs is *ca.* 40–60 nm. According to the constant Fe content in these samples, it can be assumed that the size of Fe agglomerates is constant. Therefore, grown CNTs over these sites have similar diameter.

The microstructure of CNTs was investigated with Raman spectroscopy. The Raman spectra (Fig. 11) of samples have two characteristic features of CNTs at about 1590 cm^{-1} (G band) and 1340 cm^{-1} (D band). The G band is related to vibration of sp^2 carbon–carbon bonds in the graphitic sheets of CNTs. The D band is referred to A_g mode of CNTs, representing impurities and defects in the sidewall structure of CNTs. Raman spectra indicate that multi-walled CNTs have been grown in our system rather than single-walled CNTs (SWNTs), which would give rise to a much sharper G band. This indicates that the use of Fe-doped alumina as a growth catalyst does not afford small enough Fe nanoparticles (*i.e.*, diameters <5 nm) required to yield SWNTs. Fig. 12 shows the TG/DTG curves of as-

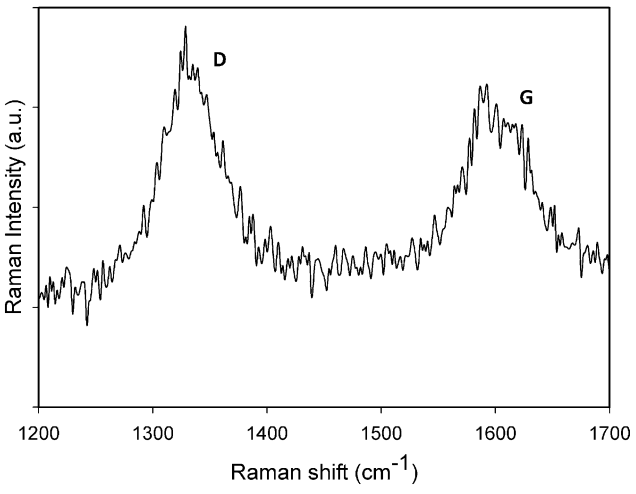

Fig. 11. Typical Raman spectrum of as-produced carbon nanotubes.

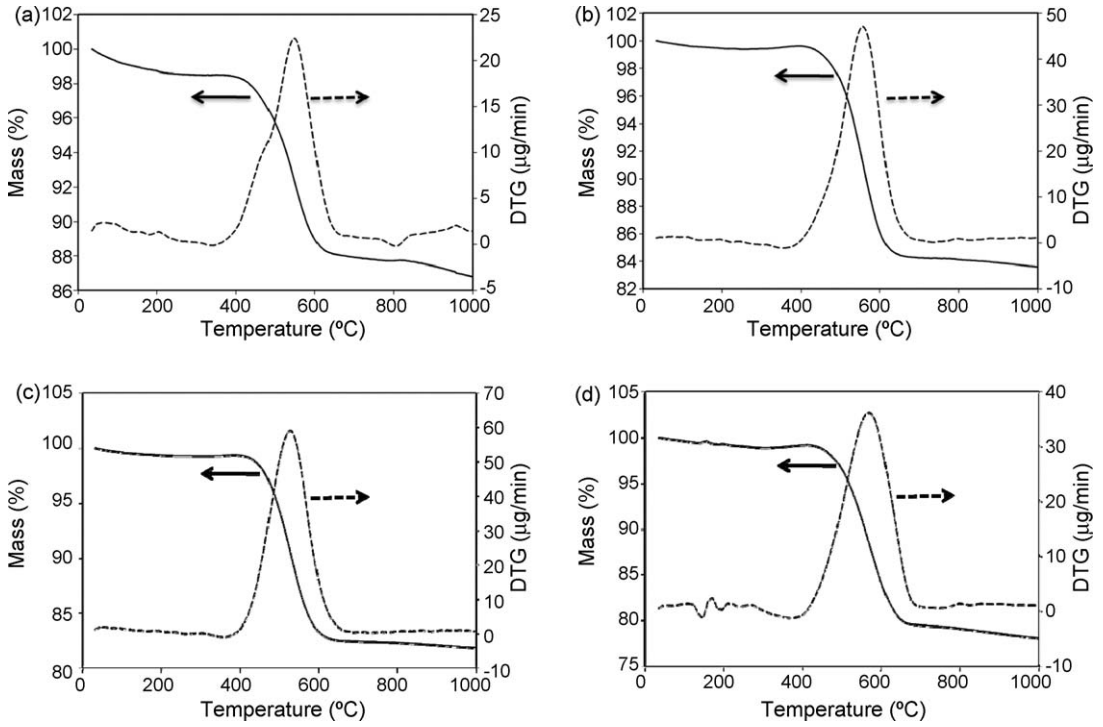

Fig. 12. TG/DTG curves of synthesized carbon nanotubes using (a) 0.02, (b) 0.05, (c) 0.07 and (d) 0.10 M [Fe] catalysts for a reaction time of 60 min.

Table 3
Percentage of carbon deposition onto different catalysts with varying iron content obtained using TG/DTG curves.

Catalyst	Carbon deposition (%)
$Fe_{0.02}$–alumina	12
$Fe_{0.05}$–alumina	16
$Fe_{0.07}$–alumina	18
$Fe_{0.10}$–alumina	21

grown CNTs. A small mass loss between 25 and 400 °C is attributed to elimination of physisorbed water and loss of surface hydroxyl groups on the alumina support. The absence of mass loss below 400 °C indicates that there is little/no amorphous carbon present in the as-grown CNTs. The major weight loss in TGA curves (above 400 °C) can be utilized for estimating the amount of CNT formation. Amount of carbon deposition was obtained by subtracting of the values for mass percent on horizontal axis of diagrams at $T < 400$ °C and $T > 500$ °C. As seen in Table 3, the amount of CNT directly depends on the iron content in alumina. Increased mass loss for $C_{0.02}NT_{60}$, $C_{0.05}NT_{60}$, $C_{0.07}NT_{60}$, and $C_{0.10}NT_{60}$ samples is consistent with SEM observations (Fig. 4) regarding the yield of AP-CNTs.

4. Conclusions

In summary, catalytic decomposition of methane over Fe-doped alumina catalysts with different iron content at 1000 °C was used to synthesize CNTs. Catalysts were characterized using N_2 adsorption–desorption measurement and XRD. Characterization of CNTs was performed using a suite of SEM, TEM, Raman spectroscopy and TGA techniques. We have concluded that multi-walled CNTs with good length and narrow diameter can be obtained with low iron concentrations in the supported catalysts during CCVD. In addition to effecting overall diameters and lengths, morphological control is also affected by varying the iron concentration of the catalyst; with increasing Fe concentrations, there is a higher propensity to grow carbon nanoribbons rather than nanotubular structures.

Acknowledgment

The authors thank the University of Tehran Research Council for support of this work. Bradley D. Fahlman would also like to thank Research Corporation (CC6690/6643) for their support of nano-materials synthesis efforts at Central Michigan University.

References

[1] S. Iijima, Nature 354 (1991) 56.
[2] M.S. Dresselhaus, G. Dresselhaus, P.C. Eklund, Science of Fullerene and Carbon Nanotubes, Academic Press, San Diego, CA, 1995.
[3] R.B. Rakhi, K. Sethupti, S. Rama Prabhu, Int. J. Hydrogen Energy 33 (2008) 381.
[4] A.C. Dillon, M.K. Jones, T.A. Bekkedahl, C.H. Kiang, D.S. Bethune, M.J. Heben, Nature 386 (1997) 377.
[5] S. Fan, M.G. Chapine, N.R. Franklin, T.W. Tombler, A.M. Cassel, H.J. Dai, Science 283 (1999) 512.
[6] P. Kim, C.M. Lieber, Science 286 (1999) 2148.
[7] J. Kong, N.R. Franklin, C. Zhou, M.G. Chapline, S. Peng, K. Cho, H. Dailt, Science 287 (2000) 622.
[8] S. Iijima, T. Ichihashi, Nature 363 (1993) 603.
[9] D.S. Bethune, G.H. Kiang, M.S. Devries, G. Gorman, R. Savoy, J. Vazquez, R. Beyers, Nature 363 (1993) 605.
[10] T. Guo, P. Nikolaev, V. Thess, D.T. Colbert, R.E. Smalley, Chem. Phys. Lett. 243 (1995) 49.
[11] H.X. Dai, P. Rinzler, P. Nikolaev, A. Thess, D.T. Colbert, R.E. Smalley, Chem. Phys. Lett. 260 (1996) 471.
[12] J.F. Colomer, G. Bister, I. Willems, Z. Konya, A. Fonseca, G. Van Tendeloo, J.B. Nagy, Chem. Commun. (1999) 1343.
[13] K.Y. Tran, B. Heinrichs, J.-F. Colomer, J.-P. Pirard, S. Lambert, Appl. Catal. A 318 (2007) 63.
[14] Y. Ando, X. Zhao, T. Sungai, M. Kumar, Mater. Today 7 (2004) 22.
[15] E. Terrado, M. Redrado, E. Muñoz, W.K. Maser, A.M. Benito, M.T. Martinez, Diamond Relat. Mater. 15 (2006) 1059.
[16] B.C. Liu, S.C. Lyu, S.I. Jung, H.K. Kang, C.-W. Yang, J.W. Park, C.Y. Park, C.J. Lee, Chem. Phys. Lett. 383 (2004) 351.
[17] M. Khodiakov, M.C. Gupta, S. Deevi, Appl. Catal. A 291 (2005) 151.
[18] D. Mehn, A. Fonseca, G. Bister, J.B. Nagy, Chem. Phys. Lett. 393 (2004) 378.
[19] B. Louis, G. Gulino, R. Vieira, J. Amadou, T. Dintzer, S. Galvagno, G. Centi, M.J. Ledoux, C. Pham-Huu, Catal. Today 102–103 (2005) 23.
[20] W. Li, H. Wang, Z. Ren, G. Wang, J. Bai, Appl. Catal. B 84 (2008) 433.
[21] Y. Wang, F. Wei, G. Luo, H. Yu, G. Gu, Chem. Phys. Lett. 364 (2002) 568.
[22] Th. Dikonimos Makris, L. Giorgi, R. Giorgi, N. Lisi, E. Salernitano, Diamond Relat. Mater. 14 (2005) 815.
[23] N. Nagaraju, A. Fonseca, Z. Konya, J.B. Nagi, J. Mol. Catal. A: Chem. 181 (2002) 57.
[24] S.L. Pirard, S. Douven, C. Bossout, G. Heyen, J.-P. Pirard, Carbon 45 (2007) 1167.
[25] B.D. Fahlman, J. Chem. Educ. 79 (2002) 203.